Comparative study on mesh-based and mesh-less coupled CFD-DEM methods to model particle-laden flow

D. Markauskas[a],[*], H. Kruggel-Emden[a],[b], R. Sivanesapillai[c], H. Steeb[c]

[a]Ruhr University Bochum, Universitätsstrasse 150, Bochum D-44780, Germany
[b]Technical University of Berlin, Ernst-Reuter Platz 1, Berlin D-10587, Germany
[c]University of Stuttgart, Pfaffenwaldring 7, Stuttgart D-70569, Germany

ARTICLE INFO

ABSTRACT

A comparative study on mesh-based and mesh-less Computational Fluid Dynamics (CFD) approaches coupled with the Discrete Element Method (DEM) is presented. As the mesh-based CFD approach a Finite Volume Method (FVM) is used. A Smoothed Particle Hydrodynamics (SPH) method represents mesh-less CFD. The unresolved fluid model is governed by the locally averaged Navier-Stokes equations. A newly developed model for applying boundary conditions in the SPH is described and validation tests are performed. With the help of the presented comparative tests, the similarities and differences of DEM-FVM and DEM-SPH methods are discussed. Three test cases, comprised of a single solid particle sedimentation test, flow through a porous block and sedimentation of a porous block, are performed using both methods. Drag forces acting on solid particles highly depend on local fluid fractions. For comparative reasons, the size of a cell in FVM is chosen such that fluid fractions match those computed in SPH. In general, DEM-FVM and DEM-SPH methods exhibit good agreement with analytic reference results. Differences between DEM-SPH and DEM-FVM approaches were found mostly due to differences in computed local fluid fractions.

© 2016 Elsevier B.V. All rights reserved.

1. Introduction

Coupled particle–fluid flow can be observed in almost all types of particulate processes. Existing approaches to model particle–fluid flow can be classified into two categories [1]: the discrete approach at microscopic level (particles are resolved as separate bodies) and the continuum approach at the macroscopic level (the fluid phase as well as the particle phase are modeled as fully inter-penetrating). In the continuum approach, macroscopic behavior is governed by balance equations (e.g. for mass and momentum) closed with constitutive relations together with initial and boundary conditions [2]. This approach is preferred in process modeling and applied research because of its computational efficiency. However, its effective use heavily depends on the constitutive relations and the model that accounts for momentum exchange between particles and fluid phase [3].

Discrete simulation approaches to model particle flow are based on the analysis of the motion of individual particles, e.g. using the Discrete Element Method (DEM), and thus inherit a reduced set of constitutive assumptions as compared to continuum approach. In this approach, the fluid phase can be modeled at the sub-particle level (Direct Numerical Simulation, DNS) such that momentum exchange (fluid–particle, particle–particle) is resolved in detail [4], or at the coarse-grained level (unresolved simulations using local volume-average technique) used for larger scale models [5]. The simulation at the sub-particle level can be used, e.g. for a detailed analysis of interaction forces that act between the fluid phase and suspended particles or for investigating the behavior of complex shaped particles dispersed in the fluid. However, such simulations are usually limited to a small number of particles [6,7]. The unresolved approach is computationally more efficient and allows simulation of much larger particle systems than DNS, while preserving discrete flow characteristics of the particles.

In most unresolved simulations mesh-based Computational Fluid Dynamics (CFD) methods are used. A Finite Volume Method (FVM) for the gas phase based on the locally averaged Navier-Stokes equations and DEM for the solid phase was first reported by Tsuji et al. [8]. Since then, a lot of investigations for the improvement of various aspects of this coupling were conducted [3,5]. A wide range of applications such as fluidized beds [9], cyclones [10], screening [11], pipeline flow [12], particle coating processes [13], pneumatic particle transport [14] and others have been discussed in

* Corresponding author.
E-mail address: markauskas@leat.rub.de (D. Markauskas).

the scientific literature. It could be concluded that DEM techniques coupled with mesh-based methods are widely recognized as state of the art in current research.

A different situation prevails when mesh-less methods are applied for the fluid phase. Coupling of DEM with the mesh-less Smoothed Particle Hydrodynamics (SPH) method was investigated only in a couple of contributions. Potapov et al. [15], Qiu [16], and Canelas et al. [17] presented a two-way coupled DEM-SPH method. Because a DNS approach was used, the method is suitable for modeling of few solid particles only. Li et al. [18] developed a SPH model for pore fluid flows through solid particle packings, however, the model does not allow for an independent movement of the fluid and solid particles. Jiang et al. [19] used SPH for modeling fluid flow in isotropic porous media, however, the solid particles representing the porous media remained static throughout the simulations. The analyses of slurry transport in SAG mills and large screens were presented in Refs.[20] and [21], where fluid flow and solid particle motion were computed using SPH and DEM, respectively. However, the model represented a one-way coupling between DEM and SPH only. Recently, a two-way coupling scheme between DEM and SPH has been derived by Gao and Herbst [22], Sun et al. [23] and Robinson et al. [24]. The application to slurry flow, abrasive wear and magnetorheological fluids were demonstrated by Cleary [25], Beck & Eberhard [26] and Lagger et al. [27] respectively. These first results look promising, however more investigations are required to clarify various aspects of DEM-SPH coupling.

In the current investigation a comparison between DEM coupled with FVM (mesh-based) and DEM coupled with SPH (mesh-less) is presented. Some of the effects influencing the motion of suspended solid particles are highlighted and the similarities/differences of solid particle motion in both methods are discussed. Sections 2, 3 and 4 describe the governing equations of the fluid and solid phases and the interaction between them. A newly developed model for boundary conditions in the SPH is described and validation tests are performed in Section 5. Three test cases, comprised of a single particle sedimentation test, flow through a porous block and sedimentation of a porous block, are performed using DEM-FVM and DEM-SPH methods whose results are discussed in Sections 6, 7 and 8.

2. Governing equations of the solid phase

The solid phase is modeled using DEM. In this method the motion of each individual solid particle $\mathcal{P}_i$ is described by Newton's second law:

$$m_i \frac{d\mathbf{u}_i}{dt} = \mathbf{F}_i^c + \mathbf{F}_i^g + \mathbf{F}_i^{int}, \tag{1}$$

where $\mathbf{u}_i$ denotes the solid particle velocity, $\mathbf{F}_i^c$ denotes the total contact force, $\mathbf{F}_i^g$ denotes the gravity force and $\mathbf{F}_i^{int}$ denotes the interaction force between solid and fluid phase. The calculation of $\mathbf{F}_i^{int}$ is described later in Section 4. The total contact force for solid particle $\mathcal{P}_i$ is obtained from the sum of contact forces acting between $\mathcal{P}_i$ and its neighboring solid particles $\mathcal{P}_j$:

$$\mathbf{F}_i^c = \sum_{j=1}^n \mathbf{F}_{ij}^c, \tag{2}$$

where n denotes the number of contacts. The contact force between solid particles is calculated as a sum of normal and tangential force components. A linear spring damper model is used for the normal component of the contact force. A linear spring limited by the Coulomb condition is used for the tangential force. A more detailed description of the used DEM model can be found in Refs.[14,28].

Discontinuities, such as an instant application of external forces, lead to spurious high-frequency oscillations in weakly-compressible SPH methods. To reduce this artifact Adami et al. [29] proposed to increase the external force gradually. In our case, the proposed technique is used for gradual increase of the gravity force acting on a solid particle:

$$\mathbf{F}_i^g = V_i \mathbf{g}[\rho_f + (\rho_s - \rho_f)\xi(t)] \tag{3}$$

where V_i denotes the volume of the solid particle, $\mathbf{g}$ denotes gravitational acceleration, ρ_f denotes fluid density, ρ_s denotes the density of the solid particle and ξ is a damping factor [29]:

$$\xi(t) = 0.5 \left[\sin\left(\pi \left(-0.5 + \frac{t}{t_{damp}} \right) \right) + 1 \right], \ t \le t_{damp}. \tag{4}$$

where t_{damp} is the predefined damping time during which the force gradually increased until the nominal value is reached.

3. Governing equations of the fluid phase

3.1. Mesh-based model

The local averaging technique [30] for the Navier-Stokes equations is applied in this research. This technique is used widely for modeling fluid–particle interaction when unresolved particle–fluid flow is considered [3,5]. The fluid phase is described in an Eulerian framework where continuity and momentum equations are given as

$$\frac{\partial \bar{\rho}_f}{\partial t} + \nabla \cdot (\bar{\rho}_f \mathbf{u}_f) = 0, \tag{5}$$

$$\frac{\partial \bar{\rho}_f \mathbf{u}_f}{\partial t} + \nabla \cdot (\bar{\rho}_f \mathbf{u}_f \otimes \mathbf{u}_f) = -\varepsilon \nabla p + \nabla \cdot (\varepsilon \boldsymbol{\tau}) - \mathbf{f}_m^{int} + \bar{\rho}_f \mathbf{g}, \tag{6}$$

where $\bar{\rho}_f = \varepsilon \rho_f$ denotes the superficial (locally averaged) density of the fluid, ε denotes the local mean fluid volume fraction, $\mathbf{u}_f$ denotes fluid velocity, p denotes pressure, $\boldsymbol{\tau}$ denotes the viscous stress tensor and $\mathbf{f}_m^{int}$ denotes the particle–fluid interaction force per unit of volume. The interaction force is further introduced in Section 4. The required porosity ε in each fluid cell is calculated as follows. Each fluid cell is divided into a number of smaller sub-cells, called a transfer grid in Ref. [31]. During the calculation the occupation of each sub-cell is checked. If the sub-cell center is inside of a solid particle, the volume of the sub-cell is marked. From the number of not marked sub-cells the approximate part of volume not occupied by solid particles is calculated for each fluid cell. This part of volume is used in Eq. (8) as the porosity of the cell. In the current study each fluid cell was divided into $40 \times 40 \times 40$ sub-cells. The presented momentum equation Eq. (8) corresponds to the model A as described by Feng and Yu [32].

For the mesh-based model a Finite Volume Method (FVM) as implemented in the commercial software ANSYS Fluent is applied. The porous media single phase model is used where the fluid is assumed as incompressible. In the performed tests neither the solid particles nor the fluid are heated. Ansys ICEM meshing software is used for the generation of meshes. The coupled analysis at each time step consists of DEM part and FVM part. The updated positions of solid particles from DEM are used for the calculation of the porosity and the interaction force. For the transfer of information about fluid velocities from the FVM and to assign the calculated porosity as well as the interaction force User Defined Functions of Fluent are utilized. More details about the used DEM-FVM coupling algorithm can be found in Ref. [31].

3.2. Mesh-less model

The Smoothed Particle Hydrodynamics (SPH) method is used as a mesh-less CFD method as an alternative approach to be coupled to the DEM. SPH is a mesh-less Lagrangian technique first introduced by Gingold and Monaghan [33] and Lucy [34] to solve problems of gas dynamics in astrophysics. Since then it has also found a widespread use in other areas of science and engineering. Its mesh-less character makes the method very flexible and enables the simulations of physical problems that might be difficult to capture by conventional mesh-based methods. The principal idea of SPH is to treat hydrodynamics in a completely mesh-free fashion, in terms of a set of sampling particles [35]. SPH particles represent a finite, lumped mass of the discretized continuum and carry information about all physical variables evaluated at their positions. Hydrodynamic equations for motion are then derived for these particles thus yielding a quite simple formulation of fluid dynamics. Mass and linear momentum are simultaneously conserved. Function values and their derivatives at a specific SPH particle are interpolated from function values at surrounding SPH particles using the interpolating (kernel) function and its derivatives. Because of the mesh-free nature of SPH, it can easily deal with problems characterized by large displacements of the fluid–structure interface, by a rapidly moving fluid free-surface and by complicated geometric settings. SPH has been applied across a broad range of engineering disciplines to compute various environmental or industrial fluid flows, for example, in marine [36], extrusion [37], geophysical [38] and coastal [39] engineering.

In a Lagrangian framework, the continuity equation and the momentum equation following Ref. [24] are used for the fluid phase:

$$\frac{D\bar{\rho}_f}{Dt} + \nabla \cdot (\bar{\rho}_f \mathbf{u}_f) = 0, \tag{7}$$

$$\frac{D\bar{\rho}_f \mathbf{u}_f}{Dt} = -\nabla p + \nabla \cdot (\varepsilon \boldsymbol{\tau}) - \mathbf{f}^{int} + \bar{\rho}_f \mathbf{g}. \tag{8}$$

Eq. (8) corresponds to model B in Refs. [3,32], in which is assumed that the pressure gradient is applied to the fluid phase only.

In the SPH method, the fluid phase is represented by separate particles. These particles carry variables such as velocity, pressure, density and mass. No connectivity is modeled between fluid particles, however, the integral representation of the function is approximated by summing up the values of the neighboring points using smooth kernel functions.

As commonly used in the weakly compressible approach to simulate incompressible fluids, an equation of state is introduced to estimate the pressure from the density field [35,40]:

$$p = \frac{\rho_0 c^2}{\gamma}\left[\left(\frac{\bar{\rho}_f}{\varepsilon\rho_0}\right)^{\gamma} - 1\right] + B, \tag{9}$$

where ρ_0 denotes the initial density of the fluid phase and c denotes the speed of sound. To keep the density to vary by at most 1% with respect to ρ_0, $c = 10 u_{max}$ is usually used [40,41], where u_{max} denotes the maximum fluid velocity magnitude. The coefficient $\gamma = 7$ is used in our simulations. B denotes a background pressure, which is set to zero in case of free surface problems, while $B > 0$ is used to avoid the tensile instability in other cases [29,40,42].

The kernel function is defined so that its value monotonously decreases as the distance between SPH particles increases. It has a compact support, the radius of which is defined by the smoothing length. The Gaussian [43], quadratic [44], cubic [45,46] and quintic

spline [47] as well as other functions can be used for this purpose. In the current research, a cubic spline [48] is used as kernel function:

$$W(r,h) = \alpha_D \begin{cases} 1 - \frac{3}{2}q^2 + \frac{3}{4}q^3, & 0 \le q < 1, \\ \frac{1}{4}(2-q)^3, & 1 \le q < 2, \\ 0, & q \ge 2, \end{cases} \tag{10}$$

where $q = r/h$, α_D is $10/(7\pi h^2)$ in case of 2D, while $1/(\pi h^3)$ in the 3D case. The smoothing length, which defines the influence area of the kernel, is denoted h. The distance between two fluid particles $\mathcal{P}_a$ and $\mathcal{P}_b$ is denoted $r_{ab} = \| \mathbf{r}_a - \mathbf{r}_b \|$.

The continuity Eq. (7) discretized using SPH and evaluated for a fluid particle $\mathcal{P}_a$ takes the form

$$\frac{D\bar{\rho}_a}{Dt} = \sum_b m_b \mathbf{u}_{ab} \cdot \nabla_a W_{ab}, \tag{11}$$

where indexes a and b indicate variables evaluated at positions $\mathbf{r}_a$ and $\mathbf{r}_b$ of fluid particles $\mathcal{P}_a$ and $\mathcal{P}_b$, respectively. m_b denotes the mass of fluid particle $\mathcal{P}_b$. $\mathbf{u}_{ab} = \mathbf{u}_a - \mathbf{u}_b$ is the relative velocity between fluid particles $\mathcal{P}_a$ and $\mathcal{P}_b$. $\nabla_a W_{ab} = \nabla_a W(r_{ab}, h)$ is the gradient of the kernel function. The summation is performed over all neighboring fluid particles (these are with index b) of fluid particle $\mathcal{P}_a$.

The momentum conservation Eq. (8) in SPH takes the form [41]:

$$\frac{D\mathbf{u}_a}{Dt} = -\sum_b m_b \left(\frac{p_a}{\bar{\rho}_a^2} + \frac{p_b}{\bar{\rho}_b^2}\right)\nabla_a W_{ab} + \mathbf{g}$$
$$+ \sum_b m_b \frac{\nu(\bar{\rho}_a + \bar{\rho}_b)}{\bar{\rho}_a \bar{\rho}_b} \cdot \frac{\mathbf{r}_{ab}\nabla_a W_{ab}}{|\mathbf{r}_{ab}|^2 + \delta^2}\mathbf{u}_{ab} + \frac{\mathbf{f}_a^{int}}{m_a}, \tag{12}$$

where $\mathbf{r}_{ab} = \mathbf{r}_a - \mathbf{r}_b$. The third term on the right-hand side in Eq. (12) is a viscous term introduced by Morris [41], where ν denotes the kinematic viscosity. δ is a small, positive number used to keep the denominator non-zero and usually set to $0.1h$. In case of solid particles approaching the fluid particle, the resulting porosity ε is decreasing and this is the cause of increased pressure in the fluid calculated by Eq. (11). Increased pressure will cause increased forces between pairs of fluid particles (see the first right term in Eq. (12)). In this way, the fluid particles are pushed away form the approaching solid particles.

$\mathbf{f}_a^{int}$ in Eq. (12) represents the solid–fluid interaction force acting on the fluid particle $\mathcal{P}_a$ due to momentum exchange with solid particles. The force $\mathbf{f}_a^{int}$ is calculated as the sum over solid particles in the domain of the fluid particle $\mathcal{P}_a$:

$$\mathbf{f}_a^{int} = \sum_i \mathbf{f}_{ai}^{int}, \tag{13}$$

$$\mathbf{f}_{ai}^{int} = -\frac{V_a W_{ai}}{\sum_b V_b W_{bi}}\mathbf{F}_i^{int}. \tag{14}$$

where V_a denotes the volume of the fluid particle $\mathcal{P}_a$ calculated as $V_a = m_a/\bar{\rho}_a$, while $\mathbf{F}_i^{int}$ is the same interaction force as in Eq. (1).

The fluid volume fraction ε_a at the position of the fluid particle $\mathcal{P}_a$ is calculated from the volumes of all solid particles $\mathcal{P}_i$ which are in the smoothing domain of the fluid particle $\mathcal{P}_a$:

$$\varepsilon_a = 1 - \sum_i V_i W_{ai}, \tag{15}$$

where V_i denotes the volume of the solid particle $\mathcal{P}_i$, while $W_{ai} = W(\| \mathbf{r}_a - \mathbf{r}_i \|, h)$ is evaluated using Eq. (10).

Special care should be taken during the calculation of the fluid fraction for the fluid particles near boundaries. If the boundary intersects the kernel domain, a part of the kernel domain is truncated by the domain boundary. This implies truncation errors in the computation of ε. To account for kernel domain truncation, the fluid fraction near boundaries is calculated by:

$$\varepsilon_a = 1 - \frac{\sum\limits_i V_i W_{ai}}{\Gamma_a} \tag{16}$$

where Γ_a is a correction factor for $\mathcal{P}_a$ as is described by Sun et al. [23]. It is an integral over the part of the kernel function which is inside of the problem domain. This modification normalizes the interpolation scheme in the vicinity of boundaries to reduce truncation errors. Originally, the Γ_a factor was proposed in Ref. [49] for the developed boundary model and was later modified in Ref. [23]. Γ_a for the cubic spline kernel is calculated from:

$$\Gamma_a = \begin{cases} -\frac{1}{60}\left(3\psi^6 - 9\psi^5 + 20\psi^3 - 42\psi - 30\right), & 0 < \psi \le 1, \\ \frac{1}{60}\left(\psi^6 - 9\psi^5 + 30\psi^4 - 40\psi^3 + 48\psi + 28\right), & 1 < \psi \le 2, \\ 1, & \psi > 2, \end{cases} \tag{17}$$

where $\psi = y/h$, y denotes the normal distance between the rigid boundary and the position of a fluid particle and h is the smoothing length as it is used in the kernel function Eq. (10).

4. Fluid–solid interaction

The interaction force $\mathbf{F}_i^{int}$ acting on solid particle $\mathcal{P}_i$ can consist from several individual solid–fluid interaction forces [3]. In the present study, the drag force $\mathbf{F}_i^D$ and the pressure gradient force $\mathbf{F}_i^{\nabla p}$ are considered as the dominant interaction forces:

$$\mathbf{F}_i^{int} = \mathbf{F}_i^D + \mathbf{F}_i^{\nabla p}. \tag{18}$$

Various models are available for the calculation of the drag force. In the current work, the correlation proposed by Di Felice [50], which is well-anticipated in literature, is used:

$$\mathbf{F}_i^D = \frac{1}{8} C_d \rho_f \pi d_i^2 (\mathbf{u}_{f,i} - \mathbf{v}_i) |\mathbf{u}_{f,i} - \mathbf{v}_i| \varepsilon_i^{2-\chi}, \tag{19}$$

where ε_i, d_i, $\mathbf{u}_{f,i}$, and $\mathbf{v}_i$ denote fluid fraction at solid particle $\mathcal{P}_i$ according to Eq. (15) or Eq. (16) near boundaries, the solid particle diameter, the fluid velocity and the solid particle velocity, respectively. ε_i is obtained from interpolating fluid fractions of surrounding fluid particles $\mathcal{P}_a$:

$$\varepsilon_i = \frac{\sum\limits_a \varepsilon_a V_a W_{ai}}{\sum\limits_a V_a W_{ai}} \tag{20}$$

The drag coefficient C_d for spherical particles is given by:

$$C_d = \left(0.63 + \frac{4.8}{\sqrt{Re_i}}\right)^2. \tag{21}$$

where $Re_i = \varepsilon_i |\mathbf{u}_{f,i} - \mathbf{v}_i| d_i / \nu$ denotes the solid particle Reynolds number and ν denotes kinematic fluid viscosity. χ is calculated as a function of the Reynolds number by

$$\chi = 3.7 - 0.65 \exp(-(1.5 - \log_{10}(Re_i))^2/2). \tag{22}$$

Provided that the pressure gradient ∇p arises only due to interaction between solid particles and fluid, F_i^D can be combined with $F_i^{\nabla p}$ [51]. The latter results in:

$$\mathbf{F}_i^{int} = \frac{\mathbf{F}_i^D}{\varepsilon} - V_i \rho_f \mathbf{g}. \tag{23}$$

$\mathbf{F}_i^{int}$ is used in Eq. (1) and Eq. (14). For the mesh-based model, i.e. Eq. (6), on the other hand, the force $\mathbf{f}_m^{int}$ acting on cell c is calculated from the drag forces $\mathbf{F}_{ci}^D$ which are acting in the cell:

$$\mathbf{f}_k^{int} = \sum\limits_i \mathbf{F}_{ci}^D / V_c , \tag{24}$$

where V_c denotes the volume of the cell.

5. Boundary conditions in SPH model

5.1. No-slip and no-penetration boundary model

The importance of accurately enforcing no-slip and no-penetration boundary conditions (BC) was discussed in Refs. [29,42,52]. Not only do BC models affect the accuracy of flow fields, but they also contribute to overall numerical stability [42]. Another aspect of boundary models in the context of the DEM-SPH method concerns the convenience of use as pointed out in Ref. [23]. In particular, it would be convenient if the geometry of the container, as defined for use in the DEM, could be directly used in SPH without further effort. To satisfy the above requirements a new variant of the BC model is proposed here. The new BC model allows container geometries to be adopted directly from the DEM model. In comparison to the BC model proposed in Ref. [23], the BC model presented here ensures no-slip conditions along the container walls.

A ghost-fluid technique is used to enforce no-slip and no-penetration boundary conditions. The ghost-fluid technique is based on the idea of modeling container walls using virtual fluid particles (ghost particles) positioned in the vicinity of container walls. Every time step these ghost particles are instantaneously generated for every fluid particle interacting with the boundary (see Fig. 1). In contrast to the classical ghost particle approach [40] where fluid particle is mirrored on the opposite side of the boundary line, in the proposed model, several ghost particles are generated instantaneously to ensure that the support of the kernel interpolants is fully contained within the fluid phase. A similar approach was used by Marrone et al. [42], however, rather than instantaneously generating ghost particles, they used pre-generated ghost particles. The instantaneous generation of ghost particles is what distinguishes the proposed BC model from other BC models proposed earlier.

As already pointed out earlier [29,52,53], a special treatment of ghost particle velocities is needed to enforce no-slip boundaries in
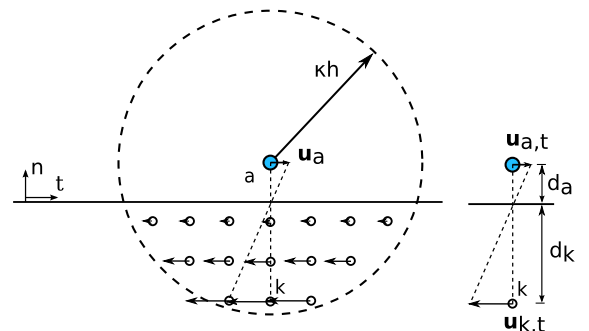

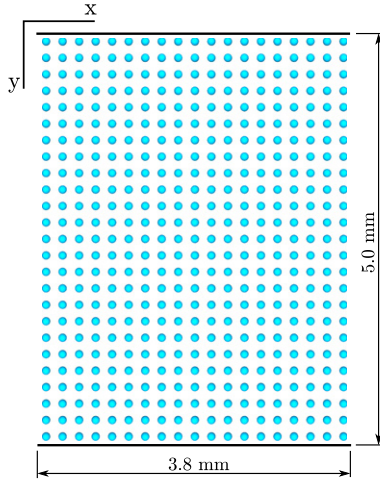**Fig. 1.** The calculation scheme of tangential boundary velocities.

Fig. 2. Initial fluid particle setup for Poiseuille flow.

Fig. 3. Poiseuille flow.

a correct way. Following Ref. [42], two velocity fields are employed. For the calculation of the viscous term in Eq. (12), the following ghost particle velocities are used:

$$\begin{cases} \mathbf{u}_{ak}^{(a)} \cdot \mathbf{t} = \left[(\mathbf{u}_a - \mathbf{u}_{bc}) \cdot (1 + \frac{d_k}{d_a}) \right] \cdot \mathbf{t}, \\ \mathbf{u}_{ak}^{(a)} \cdot \mathbf{n} = (\mathbf{u}_a - \mathbf{u}_{bc}) \cdot \mathbf{n}, \end{cases} \qquad (25)$$

where $\mathbf{u}_{ak}^{(a)}$ denotes the velocity of the k-th ghost particle relative to fluid particle a, $\mathbf{u}_{bc}$ denotes the prescribed velocity of the boundary, $\mathbf{t}$ denotes a vector tangent to the boundary and $\mathbf{n}$ is a vector normal to the boundary. Furthermore, d_k and d_a denote the normal distances of ghost particle $\mathcal{P}_k$ and fluid particle $\mathcal{P}_a$ from the container wall. For the case of free-slip $\mathbf{u}_{ak}^{(a)} \cdot \mathbf{t} = 0$ can be used. For the calculation of velocity difference in the continuity equation Eq. (11), on the other hand, the following ghost particle velocities are used:

$$\begin{cases} \mathbf{u}_{ak}^{(a)} \cdot \mathbf{t} = 0, \\ \mathbf{u}_{ak}^{(a)} \cdot \mathbf{n} = \left[(\mathbf{u}_a - \mathbf{u}_{bc}) \cdot (1 + \frac{d_k}{d_a}) \right] \cdot \mathbf{n}. \end{cases} \qquad (26)$$

Implementing two different ghost velocity fields avoids inconsistencies and loss of accuracy as discussed by De Laffe et al. [54]. In particular, using Eq. (26) in the continuity equation accounts for no-penetration whereas Eq. (25) in the momentum equation accounts for no-slip. Eitzlmayr et al. [53] have mentioned the problems of representing complex shaped geometries by discrete fluid particles and suggest a way to avoid the generation of ghost particles by use of fitted polynomial functions. In the presented BC model pre-generation of ghost particles was avoided by use of instantaneously generated ghost particles. In contrast to the use of polynomial functions that represent boundary shapes, the proposed BC model allows the use of arbitrary kernel functions without the need to adjust the BC model.

5.2. Validation tests

Two 2D tests, namely the Poiseuille flow and the flow through a periodic lattice of cylinders, are performed to validate the proposed BC model. Such or similar tests are used by many researchers to validate no-slip BCs in the SPH.

5.2.1. Poiseuille flow

The test case with two infinite parallel walls and fluid in between (Poiseuille flow) is used to verify the described boundary conditions. The fluid particles are initially at rest and driven by a body
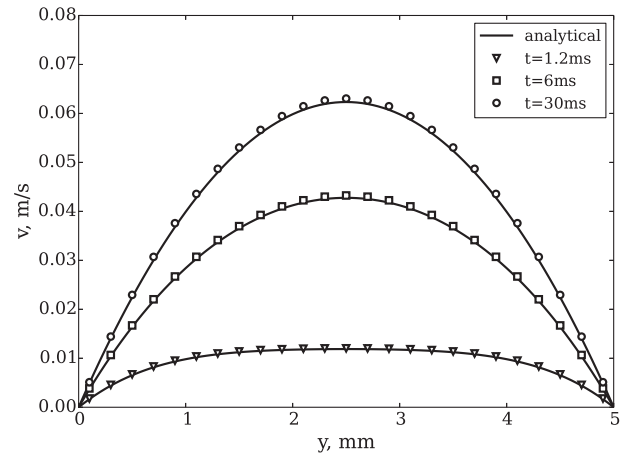
force applied in the horizontal direction. The 2D flow with 19 fluid particles in horizontal direction and 25 fluid particles in vertical direction is considered (Fig. 2). The simulation parameters as used by Eitzlmayr et al. [53] are used: the smoothing length is $h = 0.24$ mm, initial distance between fluid particles is 0.2 mm, the fluid density is $\rho = 1000 \text{kg/m}^3$, the fluid viscosity is $\mu = 0.5 \text{Pa} \cdot \text{s}$, the speed of sound (see. Eq. (9)) is $c = 10 \text{m/s}$, the body force is 10m/s^2. The analytical solution for Poiseuille flow can be found in Refs. [41,53].

The velocity profiles for the analytical and numerical SPH solutions for 1.2, 6 and 30 ms after applying the body force are presented in Fig. 3. In general, there is good agreement between the obtained results. The SPH velocities are slightly larger, than the analytical, but results correspond to the obtained values in Ref. [41] and in Ref. [53]. The velocities are approaching zero values near to the boundaries, which indicates that the no-slip condition is enforced correctly.

5.2.2. Flow through a periodic lattice of cylinders

Another test case used for validation of the presented boundary conditions is the 2D flow through a square lattice of cylinders. A single cylinder with an associated volume within the lattice is considered in the SPH (Fig. 4). As in the previous test case, the flow is driven by a body force. The periodic boundaries are applied in x and y directions, while the no-slip boundary conditions presented in Section 5.1 are applied for the cylinder. Although the used boundary
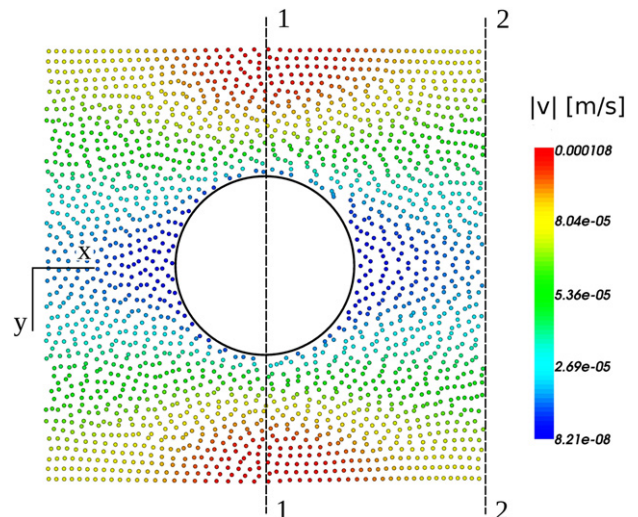

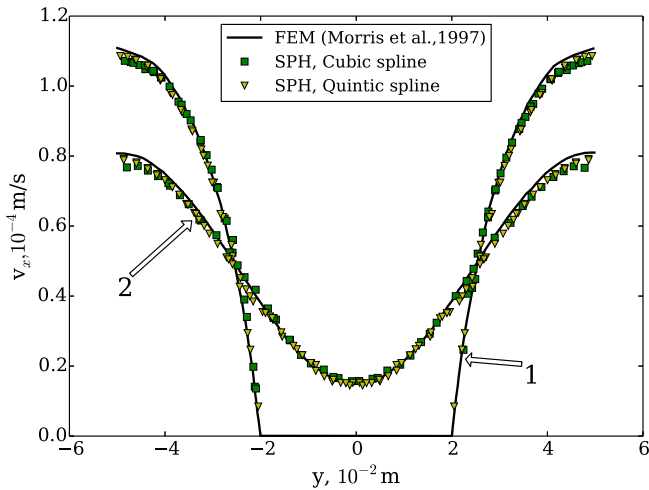Fig. 4. Fluid particle positions at t=4000s colored according to velocity magnitudes.

Fig. 5. Velocity profile along cut lines shown in Fig. 4 for flow through a periodic lattice of cylinders.

model is easy to adapt to cylindrical surfaces (simply, ghost particles could be generated below the cylinder surface following its curvature), such adaptation was not used here. The ghost particles were generated assuming a plain surface of the boundary. This simplification is reasonable in this case, because the diameter of the used cylinder is much larger than the distance between the SPH particles.

The parameters for the test case are the same as used by Morris et al. [41]: the size of the domain is 0.1×0.1 m, the initial distance between the fluid particles is 2 mm, the viscosity is $\mu = 10^{-3} \text{Pa} \cdot \text{s}$, the smoothing length is $h = 2.4$ mm, the fluid density is $\rho_f = 1000 \text{kg/m}^3$, the speed of sound is $c = 5.77 \cdot 10^{-4} \text{m/s}$, the body force is $1.5 \cdot 10^{-7} \text{m/s}^2$, the diameter of the cylinder is 4 cm. The background pressure $B = 10^{-5}$ Pa (see Eq. (9)) is used to avoid the negative pressure in the downstream flow and the formation of an unphysical void formation as a consequence. Initially the velocities of the fluid particles are zero. The fluid particles start to move due to the initiation of the body force. The velocities increase until steady state is reached. Simulations using a cubic spline (Eq. (10)) and a quintic spline kernel [41] are performed. The fluid particles at the final time $t = 4000$s colored by the velocities are shown in Fig. 4. The velocity profiles along the cut lines 1 and 2 from SPH (Fig. 4) together with the results from the steady incompressible viscous flow using a Finite Element Method (FEM) [41] are presented in Fig. 5.

The results using both kernels are close to the results obtained by FEM. The velocities with the quintic spline kernel are a little bit closer to the results obtained by FEM. This corresponds to the discussion
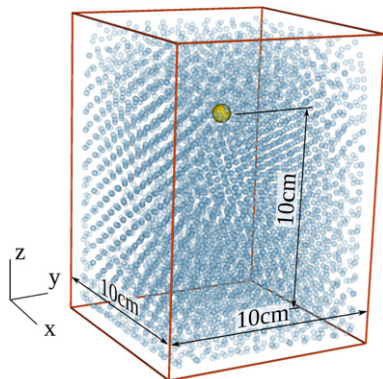
presented in Ref. [41]. However because the quintic spline is computationally more expensive, the simpler cubic spline kernel is further used in the current research.

6. Solid particle sedimentation test

To examine the performance of DEM-SPH and DEM-FVM methods, three numerical tests, starting from the settlement of one solid particle, are performed. In this single particle sedimentation test a solid spherical particle is placed in a 3D container with fluid and is realized to fall down under the influence of the gravity force. The density $\rho_f = 1000 \text{kg/m}^3$ and the viscosity $\mu = 0.001 \text{Pa} \cdot \text{s}$ are used for the fluid in both SPH and FVM methods. These physical fluid parameters are used in all following test cases. The density of the material of the solid particle is set to $\rho_s = 120 \text{kg/m}^3$. Three solid particle diameters $d = 2, 4, 8$ mm are considered in the tests. SPH particles with a smoothing length $h = 8$ mm and an initial distance $\triangle x = 5.33$ mm between them are generated in the container above the bottom wall. This gives $h/\triangle x = 1.5$, which ensures that enough neighbors are around every fluid particle [35]. In total, 8000 SPH particles are used. As an initial preparatory step, the fluid particles are allowed to settle in the container. Solid and fluid particle positions after this preparatory step are shown in Fig. 6. The boundary conditions described in Section 5.1 are used for the walls of the container.

To be able to compare the DEM-SPH and DEM-FVM, both methods should be expected to give the same (similar) results. The drag force acting onto the solid particles highly depends on the fluid fraction (see Eq. (19)). Therefore, the size of the cell in the FVM is chosen to give the same fluid fraction as in the SPH. With the current DEM-SPH setup and when the solid particle with $d = 8$ mm is used, the calculated fluid fraction during the simulation is approximately $\varepsilon = 0.935$. This gives us the cell size $0.0143 \times 0.0143 \times 0.0202$, which is used for the DEM-FVM. As a result, the container is divided into $7 \times 7 \times 6$ cells.

The velocities of the settling solid particles are shown in Fig. 7. The curves present results obtained using a one-way coupling and a two-way (full) coupling between DEM and SPH or FVM. In the one-way coupling scheme, the solid particles are experiencing the presence of the fluid, however the fluid does not "feel" the presence of the solid particles, i.e. the fluid fraction of fluid remains one and the source term on the fluid is always zero in the FVM (see Eq. 6) and in the SPH (see Eq. 8). Together with the numerical results, analytical terminal velocities of the solid particles are presented in the figure as
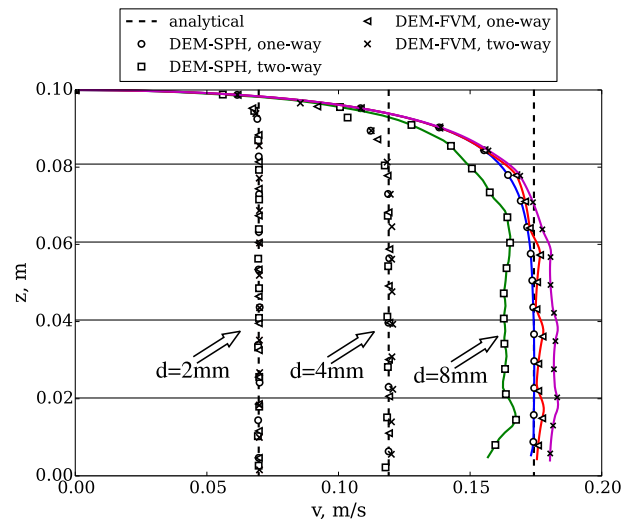

Fig. 6. Solid particle inside the container filled with SPH particles.

Fig. 7. Solid particle sedimentation velocity.

dashed vertical lines. The analytical terminal velocity was calculated from the sum of the gravity, drag and buoyancy forces, which should be equal to zero when terminal velocity is reached:

$$m\mathbf{g} + \mathbf{F}^D - V\rho_f\mathbf{g} = 0, \qquad (27)$$

where V is the volume of the solid particle. The drag force $\mathbf{F}^D$ was calculated using the same drag force correlation (Eq. (19)) as was used in the numerical methods, using the same constant fluid fraction $\varepsilon = 0.999$ for $d = 2$ mm, $\varepsilon = 0.992$ for $d = 4$ mm, $\varepsilon = 0.935$ for $d = 8$ mm as was obtained from the DEM-SPH and the fluid velocity $\mathbf{u}_f$ equal to zero. With this assumptions for the drag force, the analytical solution corresponds to the one-way coupling scheme in the numerical tests. Horizontal lines in Fig. 7 show the cell boundaries in the FVM.

In the tests with the solid particle $d = 2$ mm there are almost no difference between all 5 results (analytical, DEM-SPH one-way, DEM-SPH two-way, DEM-FVM one-way, DEM-FVM two-way). In the tests with the solid particle of $d = 4$ mm very small differences can be recognized. However the tests with a solid particle of $d = 8$ mm show differences between the calculated solid particle velocities. The obtained velocity in the DEM-SPH one-way coupling fully overlaps the line of the analytical terminal velocity. The DEM-FVM one-way result shows a bit higher solid particle settlement velocity. It is related to the way the fluid fraction is calculated on the solid particle. When the solid particle crosses a cell boundary, a part of the particle volume is assigned to one cell, while another part is assigned to another cell and, accordingly, the resultant fluid fractions are higher. Only when the particle is fully enclosed in one cell, the calculated fluid fraction corresponds to the value used in the analytical solution. This change of the fluid fraction is reflected in the waving character of DEM-FVM curve. There is interesting difference obtained between the results using two-way coupling. Because of the source term applied to the fluid in the FVM, the velocity vector in the cell, where the solid particle is, is pointing downwards. This results in a bit smaller velocity difference between the velocity of the particle and the fluid. Consequently, a smaller drag force is obtained and the particle moves a bit more quickly.
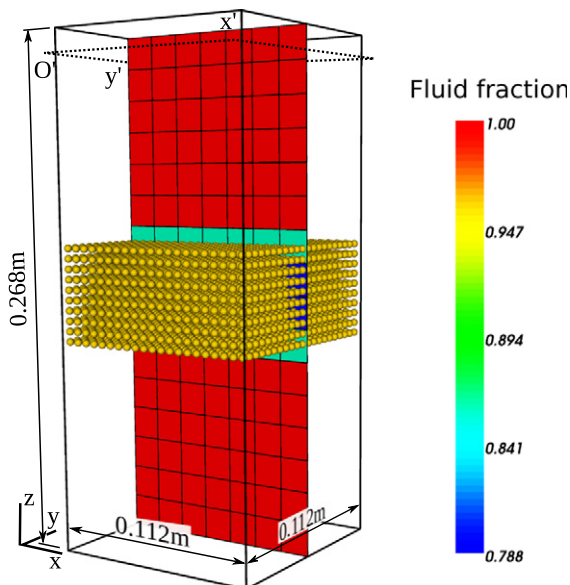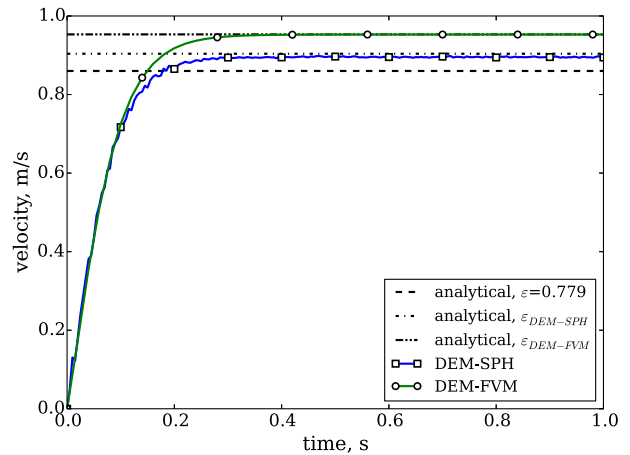

Fig. 9. Fluid flow velocities.

The opposite picture is obtained with the DEM-SPH. Here some fluid particles near the center of the solid particle move in the opposite direction then the solid particle and, therefore, a bit bigger velocity difference is obtained. Consequently, the bigger drag force is obtained and the solid particle moves slower. This result corresponds to the results reported in Ref. [24]. The authors in Ref. [24] considered settlement of a single solid particle using different fluid resolution ranging h/d from 1.5 to 6. In comparison with $2 \le h/d \le 6$, the lower settlement velocity was obtained in the case of $h/d = 1.5$. Because in our test case $h/d = 8$ mm/8 mm$= 1$, the same trend should be expected.

It should be noted, that strictly speaking the application of the local averaging technique (Eqs. (5)–(8)) for the prediction of the movement of a single solid particle is incorrect. However we used it as a test case to clarify possible differences between the DEM-SPH and DEM-FVM methods. The test cases shown in the next sections deal with the assembly of solid particles, i.e. the case the averaging technique is developed for.

7. Flow through a porous block

A numerical analysis of fluid penetrating through a fixed porous block is performed. The porous block is constructed from solid particles fixed in space. The diameter of the solid particles is $d = 4$ mm, while the distance between the solid particle centers is 5.33 mm. This gives the fluid fraction inside of the block as $\varepsilon = 0.779$. $21 \cdot 21 \cdot 10$ solid particles are used to resemble the porous block. 21,000 SPH particles with a smoothing length of $h = 8$ mm and an initial distance $\triangle x = 5.33$ mm between them are generated in the container. The container is divided into $7 \cdot 7 \cdot 16$ cells for analysis with the DEM-FVM. The block is placed in a container with fluid (see Fig. 8) and remains fixed during the simulation. The density $\rho_f = 1000$kg/m^3 and the viscosity $\mu = 0.001$Pa·s are used for the fluid. Free slip wall boundary conditions are used for sides of the container. Periodic boundaries are applied on the top and the bottom of the domain. At first, an initialization simulation is performed to reach an equilibrium state. Then, the gravity 9.81m/s^2 is applied to the fluid and simulations using both numerical methods (DEM-SPH and DEM-FVM) are performed. The fluid, which has zero velocity initially, accelerates until a constant flow velocity is reached.

Velocities obtained by the simulations together with analytically calculated velocities are shown in Fig. 9. Fluid velocities shown in Fig. 9 from FVM and SPH results were taken as average velocities on a cross plane $x'O'y'$ shown in Fig. 8. Analytical velocities are calculated from Eq. (27), however, this time, the mass m is the total mass of the
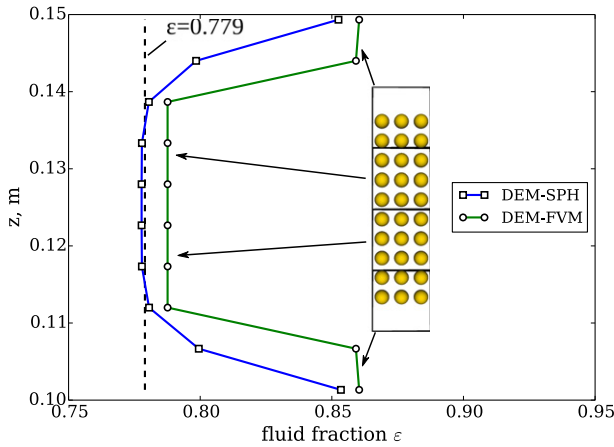

Fig. 8. Container with the porous block. The cross section of the cells is colored by the fluid fraction as obtained in the DEM-FVM.

Fig. 10. Fluid fraction inside the porous block in the DEM-SPH and the DEM-FVM.

Fig. 11. Container with the porous block (DEM-SPH) after initialization.

fluid, while $\mathbf{F}^D$ and V are the total drag force and the total volume of the solid particles respectively.

While the same porous block was used in both numerical methods, the resulting constant velocity for the DEM-FVM is 0.953m/s, but for the DEM-SPH it is 0.896m/s. Both results are higher than the analytically calculated value of 0.856m/s for $\varepsilon = 0.779$. The difference is the result of the different fluid fractions at the positions of the solid particles. As it is shown in Fig. 10, solid particle layers of the block have a bit different fluid fractions. These differences are causing the different drag forces calculated in two methods, because the calculated drag force highly depends on the fluid fraction (see Eq. (19)). The fluid velocity (Fig. 9) obtained with the DEM-FVM fully overlaps the corresponding analytical line. However small differences can be seen when comparing the DEM-SPH result with the corresponding analytical line. This difference (no more than 1%) could be caused by the influence of the walls. When the fluid fraction is less than one (situation inside of the porous block), the truncated kernels are taken into account by the use of the Γ factor in Eq. (16). Still, by the use of the Γ factor the influence of the walls is estimated only approximately. The inaccuracy made by the use of Eq. (16) decrease with the use of smaller solid particles. Additionally, the use of the Γ factor can not take into account the situation on the corners where two walls are intersecting. The result of this is a bit smaller fluid fraction near the sides of the container where the porous block is present.

8. Sedimentation of a porous block

8.1. Initialization of the specimen

Sedimentation of a constant porosity block under gravity is considered in this test. Both DEM-SPH and DEM-FVM simulations are performed. As in the previous test case, the porous block is formed from $21 \cdot 21 \cdot 10 = 4410$ solid particles with a density of 1200kg/m^3, which have the diameter $d = 0.004$m, and are placed with 0.00533m distance between their centers. The same size of container and the same number of cells for DEM-FVM and the same number of fluid particles for DEM-SPH as in the previous test case are used. However, in this test a wall is defined at the bottom, while periodic boundaries are used on the sides of the container. Initially the generated porous block is placed 20 cm above the bottom wall (Fig. 11). After generating the solid particles and the fluid cells, a steady state simulation is performed to reach an equilibrium state by DEM-FVM. In the DEM-SPH, after the generation of solid particles, the fluid particles are generated in the container. During the generation, the distances between the fluid particles are adjusted to take
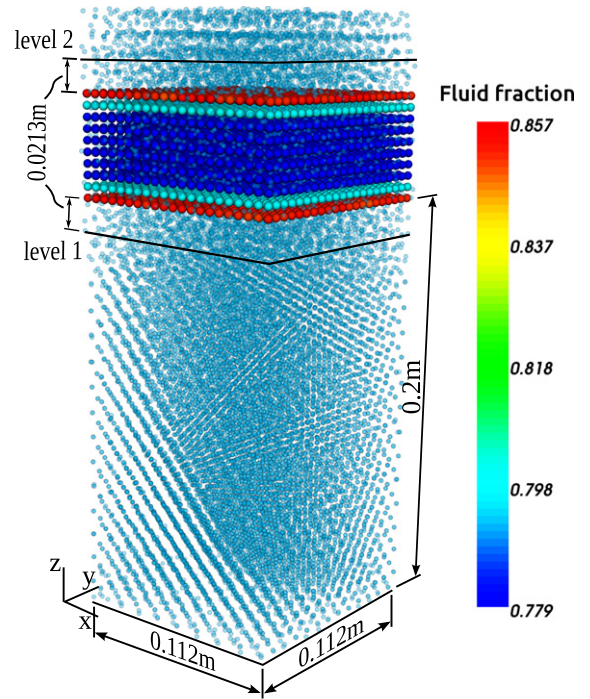
into account the lower fluid fraction inside the porous block. Then initial simulation of the system is performed by keeping the porous block unmoved. At first stage, some movement of the fluid particles are produced, because the fluid particles try to find equilibrium positions. As a result, the variation of the fluid pressure is produced. However after about 1 s, the almost constant value of the pressure is reached. It should be noted, that some level of chaotic movement of the fluid particles remains. However such movements are common for SPH [55].

After the initial simulation the resultant density distribution inside of the container simulated by the DEM-SPH is shown in Fig. 12. The superficial density $\bar{\rho}_f$ inside of the porous block is reduced because solid particles occupy volume and the fluid particles are forced to moved out from the block. The value of the superficial density is equal to $\bar{\rho}_f = \rho_f \cdot \varepsilon = 1000 \cdot 0.779 = 779$ kg/m^3 inside the center of the block. However near to the top and bottom of the block
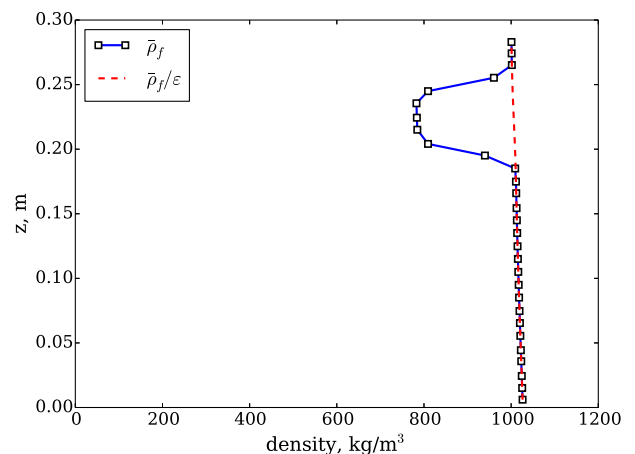

Fig. 12. Fluid density distribution at the end of the initialization procedure in the DEM-SPH.
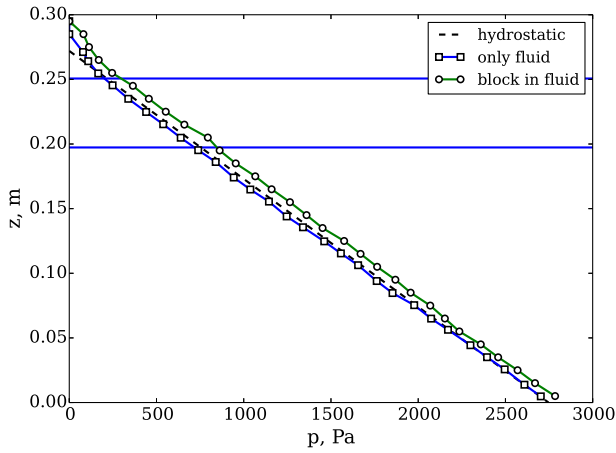
Fig. 13. Pressure in the container at the end of the initialization procedure in the DEM-SPH.

Fig. 14. Settling velocity of the porous block.

the transition domain can be seen which reflects the smooth change of the fluid fraction near the boundaries of the block. If the superficial density is divided by the fluid fraction, the physical fluid density is obtained (second line in Fig. 12). In Fig. 12 some increase of the calculated fluid density with the depth can be seen. It is because of the weakly compressible approach used in the SPH (see Eq. (9)).

The calculated pressure in the container (Fig. 13) increases from zero at the free surface to 2780 Pa near the bottom (line "block in fluid"). Additionally to the case of the container with the porous block inside (line "block in fluid") there was performed a simulation with the fluid only (line "only fluid"). As is expected the pressure is higher in case when the block is submerged in the fluid, because of the increased fluid level. However the expected difference is 115 Pa, while the calculated difference at the bottom is equal to 82 Pa only. At higher positions this difference is higher. An analytically obtained hydrostatic line ($p = \rho_f g \Delta z$) is almost overlapped by the "only fluid" line, while the "block in fluid" line keeps above however more or less parallel to it. Two horizontal lines in Fig. 13 show the top and bottom positions of the block. Bigger discrepancies from the hydrostatic line can be seen near the free surface, because of the truncated support domain of the kernel near the free surface [56].

8.2. Sedimentation step

After initialization of the specimen, the solid particles are released and they start to settle down by the influence of the gravity force. To reduce pseudo-sound waves in the fluid domain, the gravity force F_g on the solid particles is increased gradually by using Eqs. (3)–(4) with $t_{damp} = 0.5$s. Relative movements of the solid particles in the block are not allowed, therefore the particles settle down as a one solid block.

The result of the simulation of the block sedimentation by means of a settlement velocity is presented in Fig. 14. Together with the DEM-SPH and DEM-FVM results, analytically calculated curves are drawn. The analytical curves are obtained by numerically integrating the solid particle acceleration from the out-of-balance force $\mathbf{F}^{oob}$ over the time:

$$\mathbf{F}^{oob} = \mathbf{F}^g + \mathbf{F}^D + \mathbf{F}^b. \tag{28}$$

The $\mathbf{F}^D$ is calculated using Eq. (19) with $(\mathbf{u}_{f,i} - \mathbf{v}_i) = -\mathbf{v}_i/\varepsilon$, because all the fluid in the container is forced to penetrate through the porous block during its settlement. The first analytical curve is obtained by assuming a constant fluid fraction $\varepsilon = 0.779$ inside the whole block,
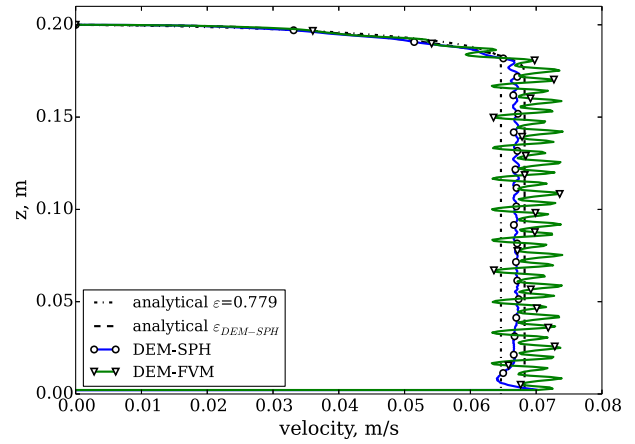
while the second analytical curve is obtained using the fluid fraction taken from the DEM-SPH, which has different values in solid particle layers near to the block boundaries. In the DEM-SPH simulation the block reaches its maximum velocity after about 0.5 s (the same time as t_{damp}, $z = 0.175$m) and moves down until it reaches the bottom wall at $t = 3.14$s. While the applied damping technique reduced the pseudo-sound waves, some waving can be seen on the block velocity curve. The influence of the bottom boundary is reflected in the last part of the curve ($z = 0 - 0.015$m).

There is a difference about 2% between the settlement velocity obtained from DEM-SPH simulation and the analytical curve even when the fluid fractions from DEM-SPH are used to obtain velocity. This difference is caused by inhomogeneous distribution of the velocities at the positions of solid particles (see Fig. 15). For example at $t = 2.3$s the drag force calculated using one velocity for the whole porous block is equal about 0.251 N, while the drag force calculated in DEM-SPH (where the drag force is calculated using the individual velocity values at each position of the solid particle) is $F^d_{DEM-SPH} = 0.262$ N. For the whole porous block $(F^g + F^b) = 0.263$N. The small difference between $F^d_{DEM-SPH}$ and $(F^g + F^b)$ equal to 0.001 N at this time step causes the small increase of velocity in the next time step.

The velocity curve of the DEM-FVM simulation shows that the block does not settle at a constant velocity, however the velocity is changing periodically. This change of the velocity is related to the change of the fluid fraction on the positions of the solid particles. The variation of the fluid fraction in the layers of the solid particles is presented in Fig. 16. When the block moves down, the calculated
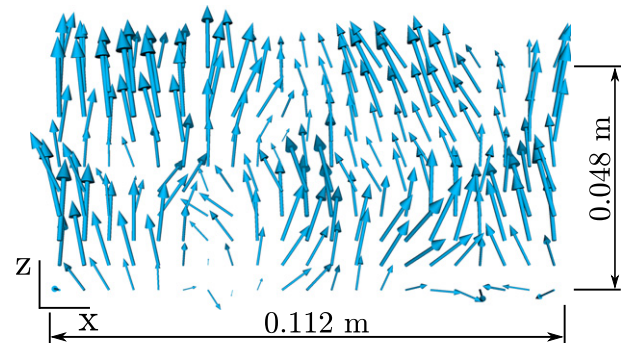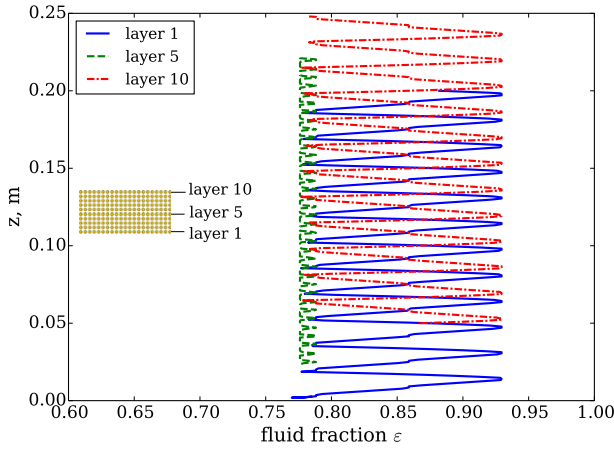

Fig. 15. Fluid velocities at positions of the solid particles at time $t = 2.3$s, $|\mathbf{u}_f|_{max} = 0.0435$m/s (DEM-SPH).

Fig. 16. The variation of the fluid fraction during the sedimentation of the porous block in the DEM-FVM.

Fig. 17. Pressures during the sedimentation of the block.

fluid fraction is changing because in the used algorithm for calculating the fluid fraction, when a solid particle crosses the boundary between two cells, its volume is divided proportionally. The fluid fraction varies a lot especially at the upper and bottom layers of the block (0.778–0.929), while in the middle the variation is between 0.776 and 0.788 only. The result of such a change of the fluid fraction is that a different total drag force is calculated. The change of the calculated fluid fraction could be reduced, if finer cells for the FVM would be used. In contrast to DEM-FVM, in DEM-SPH the fluid fraction at the positions of the solid particles is varying much less during the settlement of the block. Therefore the block in DEM-SPH moves down at a more constant velocity.

The pressures in the fluid below (level 1, Fig. 11) and above (level 2, Fig. 11) the porous block during the settlement are presented in Fig. 17. The analytical vertical line shows expected difference as is calculated from

$$\Delta p = \rho_f |\mathbf{g}| \Delta z + \frac{|\mathbf{F}^g| - |\mathbf{F}^b|}{A_s},$$

where the first term on the right side is the pressure difference due to difference in the hydrostatic pressure at level 1 and level 2. The second term reflects the pressure difference due to the drag force, which, in the case when the terminal velocity is reached, is equal to the sum of the gravity and buoyancy forces. A_s is the area of the cross section of the container. The "diff. DEM-SPH" curve shows the difference between pressures at level 1 and level 2. Quite big fluctuations can be seen in the pressures. However the difference between the expected analytical value and the averaged numerical value is about 5 % only. In contrast to DEM-SPH results, there are no fluctuations in DEM-FVM results. The resulting pressure difference ("diff. DEM-FVM" curve in Fig. 17) overlaps the analytical calculated line. It seems that the SPH method has difficulties to handle the pressure field in this case. The fluctuating pressure problem in the SPH is also reported by other researchers [57,58].

9. Conclusions

In the present work, a comparative study on mesh-based and mesh-less coupled CFD-DEM methods to model particle-laden flow was performed. The governing equations describing the coupling of the Discrete Element Method with the Smoothed Particle Hydrodynamics method were presented in detail. Comparative DEM-FVM and DEM-SPH tests were performed and similarities and differences
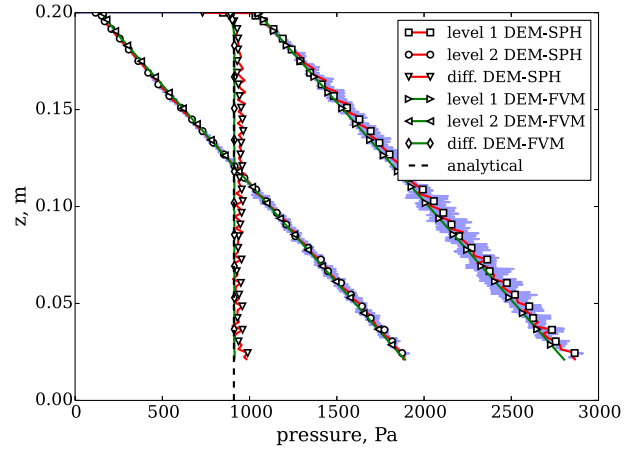
were discussed. Based on this work, the following conclusions can be drawn:

- The proposed new model to account for boundary conditions in the DEM-SPH approach was demonstrated to produce accurate results in the presented verification tests. They proved to be convenient and stable in the context of our DEM-SPH simulations.
- In general, results obtained using DEM-FVM and DEM-SPH approaches agreed well with analytic reference results. Numerical difference between DEM-SPH and DEM-FVM were found mostly due to difference in computed fluid fractions that result in different drag forces.
- In some cases, e.g. in the porous block settlement test, the DEM-FVM shows an unsmooth settlement velocity curve. This is caused by the constantly changing fluid fraction when solid particles are mapped from one cell to another. The settlement curve obtained with DEM-SPH remains smooth.
- Due to weak compressibility of the present SPH scheme, pressure fluctuations are observed during the settlement of the porous block in the DEM-SPH approach. This corresponds to the results reported by Robinson et al. [24], where an additional artificial viscosity was used to dampen these fluctuations. However, even without the artificial viscosity the mean values of fluid pressures reproduce analytical reference results with satisfactory accuracy.

References

[1] M. van der Hoef, M. van Sint Annaland, J. Kuipers, Computational fluid dynamics for dense gas–solid fluidized beds: a multi-scale modeling strategy, Chem. Eng. Sci. 59 (22-23) (2004) 5157–5165.
[2] D. Gidaspow, Multiphase flow and fluidization: continuum and kinetic theory descriptions, Academic Press, Boston, 1994.
[3] H. Zhu, Z. Zhou, R. Yang, A. Yu, Discrete particle simulation of particulate systems: theoretical developments, Chem. Eng. Sci. 62 (13) (2007) 3378–3396.
[4] K. Han, Y. Feng, D. Owen, Coupled lattice Boltzmann and discrete element modelling of fluid–particle interaction problems, Comput. Struct. 85 (11–14) (2007) 1080–1088.

[5] N.G. Deen, M. Van Sint Annaland, M. a. Van der Hoef, J. a. M. Kuipers, Review of discrete particle modeling of fluidized beds, Chem. Eng. Sci. 62 (1-2) (2007) 28–44.

[6] L. Wang, G. Zhou, X. Wang, Q. Xiong, W. Ge, Direct numerical simulation of particle–fluid systems by combining time-driven hard-sphere model and lattice Boltzmann method, Particuology 8 (4) (2010) 379–382.

[7] F. Zhao, B.G.M. Van Wachem, Direct numerical simulation of ellipsoidal particles in turbulent channel flow, Acta Mech. 224 (10) (2013) 2331–2358.

[8] Y. Tsuji, T. Kawaguchi, T. Tanaka, Discrete particle simulation of two-dimensional fluidized bed, Powder Technol. 77 (1) (1993) 79–87.

[9] D. Kafui, S. Johnson, C. Thornton, J. Seville, Parallelization of a Lagrangian–Eulerian DEM/CFD code for application to fluidized beds, Powder Technol. 207 (1-3) (2011) 270–278.

[10] J. Chen, K. Chu, R. Zou, A. Yu, A. Vince, Prediction of the performance of dense medium cyclones in coal preparation, Miner. Eng. 31 (2012) 59–70.

[11] H. Li, Y. Li, F. Gao, Z. Zhao, L. Xu, CFD-DEM simulation of material motion in air-and-screen cleaning device, Comput. Electron. Agric. 88 (2012) 111–119.

[12] K. Li, S. Kuang, R. Pan, A. Yu, Numerical study of horizontal pneumatic conveying: effect of material properties, Powder Technol. 251 (2014) 15–24.

[13] P. Darabi, K. Pougatch, M. Salcudean, D. Grecov, DEM investigations of fluidized beds in the presence of liquid coating, Powder Technol. 214 (3) (2011) 365–374.

[14] H. Kruggel-Emden, T. Oschmann, Numerical study of rope formation and dispersion of non-spherical particles during pneumatic conveying in a pipe bend, Powder Technol. 268 (2014) 219–236.

[15] A.V. Potapov, M.L. Hunt, C.S. Campbell, Liquid–solid flows using smoothed particle hydrodynamics and the discrete element method, Powder Technol. 116 (2-3) (2001) 204–213.

[16] L.C. Qiu, Numerical modeling of liquid–particle flows by combining SPH and DEM, Ind. Eng. Chem. Res. 52 (33) (2013) 11313–11318.

[17] R.B. Canelas, A.J. Crespo, J.M. Domínguez, R.M. Ferreira, M. Gómez-Gesteira, SPH-DCDEM model for arbitrary geometries in free surface solid–fluid flows, Comput. Phys. Commun. 202 (2016) 131–140.

[18] X. Li, X. Chu, D.C. Sheng, A saturated discrete particle model and characteristic-based SPH method in granular materials, Int. J. Numer. Methods Eng. 72 (7) (2007) 858–882.

[19] F. Jiang, M.S.a. Oliveira, A.C.M. Sousa, Mesoscale SPH modeling of fluid flow in isotropic porous media, Comput. Phys. Commun. 176 (7) (2007) 471–480.

[20] P.W. Cleary, M. Sinnott, R. Morrison, Prediction of slurry transport in SAG mills using SPH fluid flow in a dynamic DEM based porous media, Miner. Eng. 19 (15) (2006) 1517–1527.

[21] J.W. Fernandez, P.W. Cleary, M.D. Sinnott, R.D. Morrison, Using SPH one-way coupled to DEM to model wet industrial banana screens, Miner. Eng. 24 (8) (2011) 741–753.

[22] D. Gao, J. a. Herbst, Alternative ways of coupling particle behaviour with fluid dynamics in mineral processing, Int. J. Comput. Fluid Dyn. 23 (2) (2009) 109–118.

[23] X. Sun, M. Sakai, Y. Yamada, Three-dimensional simulation of a solid–liquid flow by the DEM-SPH method, J. Comput. Phys. 248 (2013) 147–176.

[24] M. Robinson, M. Ramaioli, S. Luding, Fluid–particle flow simulations using two-way-coupled mesoscale SPH-DEM and validation, Int. J. Multiphase Flow 59 (2014) 121–134.

[25] P.W. Cleary, Prediction of coupled particle and fluid flows using DEM and SPH, Miner. Eng. 73 (2015) 85–99.

[26] F. Beck, P. Eberhard, Predicting abrasive wear with coupled Lagrangian methods, Comput. Part. Mech. 2 (1) (2015) 51–62.

[27] H.G. Lagger, T. Breinlinger, J.G. Korvink, M. Moseler, A.D. Renzo, F.D. Maio, C. Bierwisch, Influence of hydrodynamic drag model on shear stress in the simulation of magnetorheological fluids, J. Non-Newtonian Fluid Mech. 218 (2015) 16–26.

[28] D. Markauskas, A. Kačeniauskas, The comparison of two domain repartitioning methods used for parallel discrete element computations of the hopper discharge, Adv. Eng. Softw. 84 (2015) 68–76.

[29] S. Adami, X. Hu, N. Adams, A generalized wall boundary condition for smoothed particle hydrodynamics, J. Comput. Phys. 231 (21) (2012) 7057–7075.

[30] T.B. Anderson, R. Jackson, Fluid mechanical description of fluidized beds. Equations of motion, Ind. Eng. Chem. Fundam. 6 (4) (1967) 527–539.

[31] T. Bluhm-Drenhaus, E. Simsek, S. Wirtz, V. Scherer, A coupled fluid dynamic-discrete element simulation of heat and mass transfer in a lime shaft kiln, Chem. Eng. Sci. 65 (9) (2010) 2821–2834.

[32] Y.Q. Feng, a. B. Yu, Assessment of model formulations in the discrete particle simulation of gas-solid flow, Ind. Eng. Chem. Res. 43 (26) (2004) 8378–8390.

[33] R.A. Gingold, J.J. Monaghan, Smoothed particle hydrodynamics: theory and application to non-spherical stars, Mon. Not. R. Astron. Soc. 181 (3) (1977) 375–389.

[34] L. Lucy, A numerical approach to the testing of the fission hypothesis, Astron. J. 82 (1977) 1013–1024.

[35] J.J. Monaghan, Smoothed particle hydrodynamics, Rep. Prog. Phys. 68 (8) (2005) 1703–1759.

[36] K. Shibata, S. Koshizuka, Numerical analysis of shipping water impact on a deck using a particle method, Ocean Eng. 34 (3-4) (2007) 585–593.

[37] M. Prakash, P.W. Cleary, Modelling highly deformable metal extrusion using SPH, Comput. Part. Mech. 2 (1) (2015) 19–38.

[38] R. Sivanesapillai, H. Steeb, A. Hartmaier, Transition of effective hydraulic properties from low to high Reynolds number flow in porous media, Geophys. Res. Lett. 41 (14) (2014) 4920–4928.

[39] H. Gotoh, T. Sakai, Key issues in the particle method for computation of wave breaking, Coast. Eng. 53 (2006) 171–179.

[40] A. Colagrossi, M. Landrini, Numerical simulation of interfacial flows by smoothed particle hydrodynamics, J. Comput. Phys. 191 (2) (2003) 448–475.

[41] J.P. Morris, P.J. Fox, Y. Zhu, Modeling low Reynolds number incompressible flows using SPH, J. Comput. Phys. 136 (1997) 214–226.

[42] S. Marrone, a. Colagrossi, M. Antuono, G. Colicchio, G. Graziani, An accurate SPH modeling of viscous flows around bodies at low and moderate Reynolds numbers, J. Comput. Phys. 245 (2013) 456–475.

[43] J. Monaghan, R. Gingold, Shock simulation by the particle method SPH, J. Comput. Phys. 52 (2) (1983) 374–389.

[44] R. Dalrymple, B. Rogers, Numerical modeling of water waves with the SPH method, Coast. Eng. 53 (2-3) (2006) 141–147.

[45] J. Monaghan, A. Kos, Solitary waves on a Cretan beach, J. Waterw. Port Coast. Ocean Eng. 125 (3) (1999) 145–155.

[46] M. Gómez-Gesteira, R.A. Dalrymple, Using a three-dimensional smoothed particle hydrodynamics method for wave impact on a tall structure, J. Waterw. Port Coast. Ocean Eng. 130 (2) (2004) 63–69.

[47] H. Wendland, Piecewise polynomial, positive definite and compactly supported radial functions of minimal degree, Adv. Comput. Math. 4 (1) (1995) 389–396.

[48] J. Monaghan, J. Lattanzio, A refined particle method for astrophysical problems, Astron. Astrophys. 149 (1985) 135–143.

[49] S. Kulasegaram, J. Bonet, R.W. Lewis, M. Profit, A variational formulation based contact algorithm for rigid boundaries in two-dimensional SPH applications, Comput. Mech. 33 (2004) 316–325.

[50] R. Di Felice, The voidage function for fluid–particle interaction systems, Int. J. Multiphase Flow 20 (1) (1994) 153–159.

[51] T. Oschmann, J. Hold, H. Kruggel-Emden, Numerical investigation of mixing and orientation of non-spherical particles in a model type fluidized bed, Powder Technol. 258 (2014) 304–323.

[52] A. Valizadeh, J.J. Monaghan, A study of solid wall models for weakly compressible SPH, J. Comput. Phys. 300 (2015) 5–19.

[53] A. Eitzlmayr, G. Koscher, J. Khinast, A novel method for modeling of complex wall geometries in smoothed particle hydrodynamics, Comput. Phys. Commun. 185 (10) (2014) 2436–2448.

[54] M.D. Leffe, D.L. Touzé, B. Alessandrini, A modified no-slip condition in weakly-compressible SPH, Proc. Sixth International SPHERIC Workshop, 2011, pp. 291–297.

[55] R. Sivanesapillai, N. Falkner, A. Hartmaier, H. Steeb, A CSF-SPH method for simulating drainage and imbibition at pore-scale resolution while tracking interfacial areas, Adv. Water Resour. (2016) http://dx.doi.org/10.1016/j.advwatres.2015.08.012.

[56] E.S. Lee, C. Moulinec, R. Xu, D. Violeau, D. Laurence, P. Stansby, Comparisons of weakly compressible and truly incompressible algorithms for the SPH mesh free particle method, J. Comput. Phys. 227 (18) (2008) 8417–8436.

[57] D. Molteni, A. Colagrossi, A simple procedure to improve the pressure evaluation in hydrodynamic context using the SPH, Comput. Phys. Commun. 180 (6) (2009) 861–872.

[58] M. Antuono, A. Colagrossi, S. Marrone, D. Molteni, Free-surface flows solved by means of SPH schemes with numerical diffusive terms, Comput. Phys. Commun. 181 (3) (2010) 532–549.